Near-equilibrium kinetics in the Fe(II)-silicate system and the significance of nanoparticle greenalite in Archaean Iron Formations

Sevgen, Serhat; Retzmann, Anika; Nightingale, Michael; de Obeso, Juan Carlos; Zhang, Qin; Fleming, Ian; Tostevin, Rosalie; Tosca, Nicholas J.; Tutolo, Benjamin M.

DOI
10.1016/j.gca.2025.02.015

Publication date
2025

Document Version
Final published version

Published in
Geochimica et Cosmochimica Acta

Geochimica et Cosmochimica Acta 395 (2025) 135–148

Contents lists available at ScienceDirect

Geochimica et Cosmochimica Acta

journal homepage: www.elsevier.com/locate/gca

Near-equilibrium kinetics in the Fe(II)-silicate system and the significance of nanoparticle greenalite in Archaean Iron Formations

Serhat Sevgen [a,*], Anika Retzmann [b], Michael Nightingale [a], Juan Carlos de Obeso [a,c], Qin Zhang [a,d], Ian Fleming [a], Rosalie Tostevin [e], Nicholas J. Tosca [f], Benjamin M. Tutolo [a]

[a] University of Calgary, Department of Earth, Energy and Environment, Calgary, AB, Canada
[b] University of Calgary, Department of Physics and Astronomy, AB, Canada
[c] University of Utah, Department of Geology and Geophysics, Salt Lake City, UT, USA
[d] Delft University of Technology, Department of Geoscience and Engineering, Delft, Netherlands
[e] University of Cape Town, Department of Geological Sciences, Cape Town, South Africa
[f] University of Cambridge, Department of Earth Sciences, Cambridge, UK

ARTICLE INFO

Associate Editor: Jeffrey G. Catalano

Keywords:
Greenalite
Banded iron formations
Si isotope doping
Precambrian ocean chemistry
Nanoparticles

ABSTRACT

As the products of chemical sedimentation in the Archean oceans, Banded Iron Formations (BIFs) have been interpreted to record (bio)geochemical transitions in Earth's ancient biosphere. Nonetheless, the effects of diagenesis and metamorphism over the long history of these rocks make it difficult to identify the minerals involved in the earliest stages of BIF formation. A series of recent studies has suggested that greenalite ($Fe_3^{2+}Si_2O_5(OH)_4$), formed through hydrothermal fluid-seawater interactions, was among the primary mineral components of BIFs. However, the reactivity of greenalite as a function of relevant environmental parameters has not yet been mechanistically studied. The plausibility of its role in forming BIF deposits therefore remains speculative. Here, we fill this knowledge gap by conducting a series of kinetic experiments using a novel Si isotope doping method with hydrated, amorphous Fe(II)-silicate (a precursor to crystalline greenalite). The advantage of this technique is that it permits simultaneous determination of near-equilibrium forward and reverse reaction rates of Fe(II)-silicate-fluid interaction in plausible Archean ocean compositions. Reaction rate calculations indicate that the system's behavior is governed by Fe(II)-silicate saturation state, with SiO_2 sorption becoming dominant once a saturation threshold is exceeded. Combining kinetic data and thermodynamic calculations for the Fe-silicate-seawater system permits determination of a new solubility product for amorphous Fe(II)-silicate as $\log(K) = 24.9 \pm 0.25$. This value indicates maximum Fe^{2+} concentrations in Archean ocean waters at 25 °C would range from ~ 1 mmol/kg at pH 7 to ~ 10 μmol/kg at pH 8. Combining these observations with calculations of Stokes' settling velocity implies that long-distance transport of greenalite nanoparticles – *e. g.,* from deep-ocean hydrothermal vent sources to loci of BIF deposition – would have been feasible. Coupled with SiO_2 sorption behavior on greenalite surfaces and the background SiO_2 flux associated with the unique styles of Archean chert deposition, these results suggest that periodic waxing and waning of greenalite nanoparticle transport to BIF depositional environments can help to explain the Fe- and Si-enriched layers preserved in BIFs. Our results also provide a mechanistic underpinning for the exceptional preservation of greenalite in Archean sediments and its frequent association with chert. Ultimately, the readiness with which greenalite would have precipitated from Archean seawater and its apparent ability to be preserved despite transport across ocean basins suggests that it is time to reassess the traces of Earth's early oceans recorded in BIFs and the ways in which these may be interpreted in light of new depositional models.

1. Introduction

Banded Iron Formations (BIFs) are considered a unique record of the (bio)geochemical transitions that occurred in Earth's ancient oceans (Bekker et al., 2013; Conley et al., 2017; Fischer and Knoll, 2009; Halevy et al., 2017; Jiang and Tosca, 2019; Johnson et al., 2003, 2013, 2022a;

* Corresponding author.
E-mail address: serhat.sevgen@ucalgary.ca (S. Sevgen).

https://doi.org/10.1016/j.gca.2025.02.015
Received 30 January 2025; Accepted 12 February 2025
Available online 15 February 2025

Klein, 2005; Konhauser et al., 2017; Konhauser and Knoll, 2009; Konhauser et al., 2017; Maliva et al., 2005; Rasmussen et al., 2021; Robbins et al., 2015, 2016; Siever, 1992; Tosca et al., 2019; Tostevin and Ahmed, 2023; Trendall, 2002). BIFs are marine sedimentary rocks formed mostly during Neoarchaean and Palaeoproterozoic Eras (Bekker et al., 2013). They originally precipitated from anoxic and Fe-rich seawater as alternating layers of Fe minerals with chert (Klein, 2005; Konhauser et al., 2017; Johnson et al., 2022a; Rasmussen et al., 2021). The Archean and Early Proterozoic oceans experienced a greater degree of hydrothermal cycling relative to their modern counterparts due to higher early mantle temperatures (Isley, 1995). The Fe for BIF genesis has been associated with hydrothermal vents (Isley, 1995; Isley and Abbott, 1999; Kump and Seyfried, 2005; Muhling et al., 2023; Sylvestre et al., 2017; Tosca and Tutolo, 2023; Viehmann et al., 2015). Likewise, these vents, along with contemporaneously elevated seawater Si concentrations, are thought to have served as principal sources of silica.

Although numerous mechanisms have been proposed to explain the transformation of hydrothermal Fe into precursor phases of BIFs, the processes connecting hydrothermally emitted Fe to mineral precipitation and BIF genesis remain subject of substantial debate (Halevy et al., 2017; Fischer and Knoll, 2009; Hinz et al., 2021; Johnson et al., 2022a, 2022b; Konhauser et al., 2017; Muhling and Rasmussen, 2020; Posth et al., 2013; Rasmussen et al., 2015, 2021, 2024a; Rasmussen and Muhling, 2022; Sun et al., 2015; Tosca et al., 2016, 2019; Tosca and Tutolo, 2023; Tostevin and Sevgen, 2024). Accurately determining the nature of the BIF-forming primary Fe minerals is thus key to understanding a principal Fe sink and its impact on geochemical interactions and the redox state of the Archean ocean–atmosphere system.

Traditional models suggest that the originally deposited Fe-bearing minerals were Fe oxide phases which were converted from hydrothermal Fe^{2+} to Fe(III)-oxyhydroxides as a result of different Fe oxidation pathways in the surface ocean conditions (Konhauser et al., 2017 and references therein). However, in recent years, an alternative model for BIF genesis has been gaining momentum in the geoscience community. This model proposes a new set of mechanisms to suggest a major role of hydrothermal Fe^{2+} precipitation, primarily as a Fe(II)-silicate, in BIF deposition (Rasmussen et al., 2021, 2024a; Rasmussen and Muhling, 2021; Tosca and Tutolo, 2023). Using high-resolution electron microscopy investigations of particles locked in chert layers, recent studies have indicated that greenalite ($Fe_3^{2+}Si_2O_5(OH)_4$) was among the originally precipitated BIF sediments (Muhling and Rasmussen, 2020; Johnson et al., 2018; Rasmussen et al., 2014, 2015, 2016, 2017, 2021; Rasmussen and Muhling, 2021). Therefore, greenalite nanoparticles which were circulated and subsequently deposited because of hydrothermal fluid-seawater interactions in anoxic Archean water conditions (Rasmussen et al., 2019a; Tosca and Tutolo, 2023) could be an important contributor to BIF formation along with other suggested minerals such as Fe oxyhydroxides and green rust (mixed valence Fe-rich double layer hydroxides) (Konhauser et al., 2017; Johnson et al., 2022a; Halevy et al., 2017). Nanoparticulate greenalite has historically gone undetected during petrographic investigations because it is often below the resolution of standard imaging techniques (Rasmussen et al., 2021; Rasmussen and Muhling, 2022).

Fe-bearing nanoparticles have been found in present-d ay hydrothermal vents across Earth's ocean basins (Findlay et al., 2019; Fitzsimmons et al., 2017; Gartman et al., 2019; Yücel et al., 2011; Yücel et al., 2021). These particles are predominantly Fe-sulfides (*e. g.,* pyrite) as well as Fe oxyhydroxides, partly due to the SO_4^{2-}- and O_2-rich nature of modern seawater. However, the chemical compositions of Archean oceans differed substantially from the oceans today (Halevy and Bachan, 2017). In particular, ancient seawater contained elevated concentrations of dissolved SiO_2 (Conley et al., 2017; Maliva et al., 2005; Siever, 1992) and Fe (Poulton and Canfield, 2011; Rasmussen et al., 2015) but had substantially lower concentrations of SO_4^{2-} and O_2 (Crowe et al., 2014; Jamieson et al., 2013; Kump and Seyfried, 2005; Lyons et al., 2024). The pH of Archean seawater is thought to have varied over the range of ~ 6.0–7.5 (Halevy and Bachan, 2017; Krissansen-Totton et al., 2018), further highlighting the distinct chemical conditions of ancient oceans. Tosca and Tutolo (2023) calculated that mixing hot, Fe-rich hydrothermal fluids with silica-rich, sulfate-free, anoxic Archean deep-sea waters precipitates greenalite as it becomes thermodynamically supersaturated. An experimental study by Tosca et al. (2016) also showed that hydrated, amorphous Fe(II)-silicate (Fe(II)-silicate hereafter), a precursor phase to crystalline greenalite, with very small particle size (on the nanometer scale) can rapidly nucleate in anoxic seawater at 25 °C. Upon precipitation and dehydration, Fe(II)-silicate can crystallize into the greenalite nanoparticles that are preserved in the BIF samples today (Rasmussen et al., 2021). However, the reactivity and stability of this Fe(II)-silicate phase under conditions resembling those of Archean oceans remains poorly constrained.

As discussed above, the Archean oceans are widely agreed to have been rich in dissolved Fe^{2+} and SiO_2 (Conley et al., 2017; Maliva et al., 2005; Siever, 1992; Poulton and Canfield, 2011; Rasmussen et al., 2015) such that Archean seawater may have been in approximate equilibrium with respect to greenalite or its precursor (Jiang and Tosca, 2019; Tosca et al., 2016). As a result, investigations of the reactivity of Fe(II)-silicate in Archean ocean waters require examination of the rates and directions of Fe(II)-silicate reactions at near-equilibrium conditions. However, examining near-equilibrium kinetics poses numerous challenges. For example, mineral reaction rates are typically measured by tracking changes in the concentration of a specific element (*e. g.,* Si, Fe, etc.) over time. Unfortunately, at near-equilibrium conditions, these changes are often less than the uncertainty of the analytical technique used and thus difficult to detect (Nagy et al., 1991; Nagy and Lasaga, 1992; Rimstidt, 1997). Moreover, near-equilibrium solutions are impacted by both forward and reverse reactions and may also be supersaturated with respect to secondary mineral phases. Secondary mineral precipitation alters the solution chemistry and complicates the retrieval of primary reaction rates based only on concentration changes over time (Gruber et al., 2013; Zhu et al., 2016).

The recently developed technique known as Si isotope doping presents unique opportunities to combat the inherent difficulty in determining near-equilibrium silicate-water reaction rates (Gruber et al., 2013; Liu et al., 2016). This methodology most typically involves experimental reaction of solid materials composed of silicon with natural isotopic abundances (^{28}Si: 0.9223, ^{29}Si: 0.0468 and ^{30}Si: 0.0309) and an experimental fluid enriched in one of the scarce isotopes (*e. g.,* ^{29}Si or ^{30}Si). Analysis of the change in isotopic concentrations in the fluid over time permits simultaneous determination of forward and reverse reactions rates (*i.e.,* precipitation and dissolution rates) at near-equilibrium conditions (Che et al., 2021; Gong et al., 2019; Gruber et al., 2013; Schott et al., 2024; Zhu et al., 2016; Zhu et al., 2021). With this method, (i) reaction rates can be determined even if the total concentration change is small and (ii) secondary phase precipitation during experiments does not significantly alter the isotopic ratios of the fluid, allowing the primary reaction rate to be calculated even if secondary minerals are also forming (Zhang et al., 2020; Che et al., 2021; Zhu et al., 2016; Zhu et al., 2021).

In this study, we examine the kinetics of reactions between Fe(II)-silicate and Archean seawater at near-equilibrium conditions using this Si isotope doping method. We investigate the effects of solution saturation – the interplay of solution pH, Fe^{2+} and SiO_2 concentration – on Fe(II)-silicate reactivity through a series of batch experiments. By combining time-series silicon isotope data with thermodynamics- and kinetics-based geochemical calculations, we provide a comprehensive dataset that bears directly on the hypothesis that greenalite may represent the primary Fe^{2+} precursor mineral in BIFs. The resultant dataset also permits new estimates of the maximum Fe concentration in Archean oceans on the basis of observed greenalite stability in BIF deposits.

2. Experimental methods

Our experimental procedure employed two main steps to accurately track the near-equilibrium reaction kinetics of Fe(II)-silicate system (for a schematic of the experimental procedure, see Fig. S1). First, Fe(II)-silicate was synthesized as a starting material, and, subsequently, this synthesized Fe(II)-silicate was used in the Si doping experiments to evaluate its reactivity. All experiments were conducted under anoxic conditions in a Coy polymer anaerobic chamber. The anoxic environment was maintained by a Pd catalyst that circulated the anaerobic chamber's atmosphere and maintained gas levels of approximately 97.5 % nitrogen and 2.5 % hydrogen. The Pd catalyst removed oxygen from the anaerobic chamber by continuously reacting oxygen with hydrogen gas to form water, which is quickly absorbed by co-located desiccants. Following the doping experiments, fluid chemistry analyses were employed to calculate dissolution and precipitation rates.

2.1. Synthesis of Fe(II)-silicate

A modified procedure after Tosca et al. (2016) was used to synthesize the Fe(II)-silicate. Acid-cleaned Low-Density Polyethylene (LDPE) bottles were used in the synthesis experiment. All bottles were triple wrapped with aluminum foil to prevent photo-oxidation of Fe^{2+}. The bottles were filled with 18 MΩ deionized (DI) water and purged with N_2 gas for approximately two hours to remove dissolved O_2 (Butler et al., 1994). Once purged, they were immediately transferred to the anaerobic chamber and continuously stirred for 48-hours in the anaerobic chamber to degas any remaining O_2 and equilibrate with the anoxic atmosphere. All solutions were prepared by using American Chemical Society (ACS) reagent-grade chemicals. Sodium metasilicate nonahydrate ($Na_2SiO_3{\cdot}9H_2O$) was added to one container to reach a concentration of ~ 7 mmol/kg dissolved Si, and then the pH of the solution was adjusted to ~ 12 by using freshly prepared 1 mol/L NaOH. The Fe^{2+} solution was freshly prepared from $FeCl_2{\cdot}4H_2O$ and DI water to reach a concentration of ~ 7 mmol/kg Fe^{2+} and then adjusted to pH ≈ 2.8 using 1 mol/L trace metal grade HCl. Both solutions were prepared without sulfate and carbonate ions, in accordance with constraints established by previous studies for Archean seawater (Crowe et al., 2014; Jamieson et al., 2013; Jiang and Tosca, 2019). The pH measurements were performed using a Thermo Scientific™ PerpHecT™ Orion™ ROSS™ combination pH microelectrode, calibrated daily using NIST-traceable pH 4, 7, and 10 buffers. The Fe(II)-silicate precipitation process was conducted by titrating the Fe^{2+} solution with the SiO_2 solution using a peristaltic pump at a constant flow rate of 6.5 x 10^{-2} g/min. Fluid samples were taken over time (minutes to days) to quantify the fluid evolution through fluid mixing and Fe(II)-silicate precipitation. The fluid composition data for the precipitation experiment is provided in the Supplementary Material. Samples were collected using a syringe and filtered through 0.45-μm Millipore PVDF syringe filters before being preserved with trace metal grade HCl for subsequent analysis. After ~ 10 days, the precipitation experiment was terminated, and the experimental solution was filtered with a vacuum filtration system through 0.22 μm Durapore PVDF filter to collect the precipitated particles in the anaerobic chamber. Collected solids were washed three times with O_2-free DI water to remove any remaining experimental solution and they were allowed to dry overnight within the glovebox at room temperature in Al foil wrapped containers.

2.2. ^{29}Si isotope doping

The ^{29}Si stock solution was prepared by dissolving $^{29}SiO_2$ powder (from IsoFlex USA, San Francisco, California) with an isotopic enrichment of ≥ 99.69 % in DI water in a LDPE bottle. The powder had an isotopic composition of ^{28}Si (0.0004), ^{29}Si (0.999) and ^{30}Si (0.0006). The solution pH was adjusted to a value > 11 using freshly prepared 1 mol/L NaOH, before being placed in an oven for 48 h at 60 °C to assure complete dissolution of the $^{29}SiO_2$ powder. The solution was then left to reach room temperature and purged with N_2 gas for two hours to remove dissolved O_2 (Butler et al., 1994) before being placed in the anaerobic chamber to further degas for 48 h. Then, pH was adjusted to the working pH for each experiment using 1 mol/L HCl (Table 1). In another LDPE bottle (triple wrapped with Al foil), ^{29}Si solution was mixed with enough freshly prepared 1 mol/kg $FeCl_2{\cdot}4H_2O$ solution to achieve the working Fe^{2+} concentration for the doping experiments (Table 1). Four distinct doping experiments (Exp. I, Exp. H, Exp. Q, and Exp. D) were conducted to investigate the influence of saturation state on Fe(II)-silicate reaction kinetics. The initial conditions of each experiment were carefully adjusted to reflect variations in the saturation state as a function of starting Fe^{2+} and Si concentrations and pH. For instance, the starting pH, Si concentration, and Fe^{2+} concentration in Exp. I were 7.68, 1.24 mmol/kg, and 0.11 mmol/kg, respectively, whereas for Exp. H, they were 7.03, 0.37 mmol/kg, and 0.50 mmol/kg, respectively. Additional details regarding the evolution of fluid chemistry throughout the isotope doping experiments are provided in Table 1. All data for the Si isotope doping experiments is provided in the Supplementary Material. The procedure for the ^{29}Si doping experiments was based on the methods detailed by Che et al. (2021). The experiments were conducted at room temperature by reacting the dry Fe(II)-silicate with the ^{29}Si-Fe^{2+} solution. The Fe(II)-silicate is characterized by natural Si isotopic abundances (^{28}Si: 0.9223, ^{29}Si: 0.0468 and ^{30}Si: 0.0309), and the sharp difference in isotopic composition between Fe(II)-silicate and reacting fluid (^{28}Si: 0.0004, ^{29}Si: 0.999 and ^{30}Si: 0.0006) thus permits monitoring of reaction progress by tracking the change in Si isotopic composition in the fluid over time (Che et al., 2021). All experiments were conducted in 1.5 mL acid-cleaned microcentrifuge tubes triple wrapped with Al foil, containing 7.5 mg (Exp. H, Exp. Q, and Exp. D) and 15 mg (Exp. I) Fe(II)-silicate. The ^{29}Si-Fe^{2+} solution was injected into the microcentrifuge tubes and shaken by hand to promote contact between the solids and the solution. This experimental procedure was repeated without using Fe(II)-silicate in the microcentrifuge tubes containing only ^{29}Si-Fe^{2+} solution as a control (referred to as blank experiments hereafter). The reactions were stopped at periodic times by removing the fluid via syringe and sacrificing individual microcentrifuge tubes. Approximately 1 mL fluid was filtered through a 0.22 μm Millipore PVDF syringe filter and diluted with DI water and acidified with trace metal grade HCl for subsequent fluid analysis. The pH of the remaining fluid in the microcentrifuge tubes was then measured. The collection of the fluids from microcentrifuge tubes combined with the analysis of the starting solution permits calculation of both the dissolution and precipitation rate by comparing changes in Si concentration and isotopic composition throughout the experiment.

Total Si concentration change with respect to time in a batch experiment may be evaluated via (Rimstidt, 2014):

$$\frac{d[Si]}{dt} = \frac{V_{Si,dis}.A.R_{dis} - V_{Si,pre}.A.R_{pre}}{M} \quad (1)$$

where d[Si] is change in the total Si concentration (mmol/kg) in the solution over the time interval Δt (s), $V_{Si,dis}$ and $V_{Si,pre}$ represent the stoichiometric coefficient of Si within the reactants and the products of the reaction, respectively, A is the surface area of the reacting mineral (m^2), R_{dis} and R_{pre} are the dissolution, and the precipitation rates (mol/m^2/s), respectively and M represents the solution mass (kg) within the batch reactor. Given the inherent challenges in quantifying specific surface area of the Fe(II)-silicate without oxidation and accompanying changes to its surface properties, we use m (mineral mass) instead of A to normalize dissolution and precipitation rates.

We can rewrite this general formula for ^{28}Si and ^{29}Si following the approach described in Gruber et al. (2013):

$$\frac{d[^{28}Si]}{dt} = \frac{V_{Si,dis}.m.R_{dis}.\left(\frac{[^{28}Si]}{[Si]}\right)_{dis} - V_{Si,pre}.m.R_{pre}.\left(\frac{[^{28}Si]}{[Si]}\right)_{\bar{t}}}{M} \quad (2)$$

Table 1
Solution chemistry and calculated results of silicon doping experiments. All solutions contain 55 mmol/kg NaCl.

Name	Time (min)	pH	^{28}Si (mmol/kg)	^{29}Si (mmol/kg)	∑Si[a] (mmol/kg)	Fe (mmol/kg)	Fe $(OH)_2$ (SI)	Greenalite[b] (SI)	Greenalite[c] (SI)	SiO_2 (am) (SI)	Log Q (Greenalite)	Rdis ($x10^{-9}$) (mol/g/s)	Rpre ($x10^{-9}$) (mol/g/s)
Exp. I-0	0	7.68	0.03	1.16	1.24	0.11	−1.84	4.68	−0.25	−0.18	27.36		
Exp. I-1	49*	7.30	0.15	0.91	1.10	0.46	−1.99	4.14	−0.79	−0.23	26.82	2.60	4.86
Exp. I-2	268.3*	7.34	0.23	0.70	0.97	0.48	−1.89	4.34	−0.59	−0.29	27.01	0.54	1.06
Exp. I-3	1302	7.24	0.31	0.51	0.86	0.55	−2.03	3.79	−1.14	−0.34	26.47	0.15	0.24
Exp. I-4	3703.5*	7.27	0.36	0.30	0.70	0.57	−1.95	3.84	−1.09	−0.44	26.51	0.09	0.15
Exp. I-5	6990	7.17	0.38	0.26	0.67	0.54	−2.17	3.15	−1.78	−0.45	25.83	0.02	0.03
Exp. I-6	10181	7.22	0.39	0.12	0.55	0.59	−2.04	3.37	−1.56	−0.54	26.04	0.11	0.13
Exp. I-7	15677	7.25	0.39	0.10	0.52	0.56	−2.00	3.44	−1.50	−0.56	26.11	0.01	0.02
Exp. I-8	20240	7.24	0.39	0.08	0.49	0.53	−2.04	3.28	−1.65	−0.58	25.95	0.02	0.02
Exp. I-9	25745	7.18	0.39	0.07	0.48	0.53	−2.16	2.91	−2.02	−0.59	25.59	0.01	0.01
Exp. H-0	0	7.03	0.02	0.33	0.37	0.50	−2.49	1.71	−3.22	−0.70	24.38		
Exp. H-1	54	6.75	0.17	0.27	0.46	0.87	−2.81	0.93	−4.01	−0.60	23.60	5.84	2.71
Exp. H-2	170	6.77	0.29	0.23	0.54	0.88	−2.76	1.21	−3.72	−0.54	23.88	2.59	1.44
Exp. H-3	1551	6.84	0.52	0.17	0.71	0.88	−2.63	1.86	−3.07	−0.42	24.53	0.53	0.29
Exp. H-4	3179	6.80	0.64	0.14	0.81	0.94	−2.67	1.83	−3.11	−0.36	24.50	0.35	0.25
Exp. H-5	6050	6.81	0.67	0.12	0.81	0.87	−2.69	1.78	−3.15	−0.36	24.45	0.11	0.11
Exp. H-6	8476	6.83	0.68	0.11	0.81	0.84	−2.67	1.85	−3.08	−0.36	24.52	0.05	0.05
Exp. H-7	11167	6.85	0.68	0.11	0.81	0.86	−2.62	2.00	−2.93	−0.36	24.68	0.01	0.01
Exp. Q-0	0	7.70	0.02	1.01	1.06	0.11	−1.83	4.60	−0.33	−0.25	27.28		
Exp. Q-1	62	6.96	0.16	0.87	1.06	0.40	−2.72	1.91	−3.02	−0.24	24.58	4.42	4.52
Exp. Q-2	180	6.91	0.29	0.74	1.06	0.48	−2.75	1.84	−3.09	−0.24	24.51	2.62	2.65
Exp. Q-3	2282.5*	6.90	0.56	0.48	1.07	0.63	−2.65	2.15	−2.78	−0.24	24.82	0.42	0.39
Exp. Q-4	5968	6.93	0.73	0.30	1.06	0.57	−2.63	2.18	−2.75	−0.24	24.86	0.27	0.26
Exp. Q-5	8396	6.96	0.73	0.26	1.02	0.51	−2.62	2.19	−2.74	−0.26	24.86	0.10	0.12
Exp. Q-6	11085	7.00	0.74	0.25	1.03	0.51	−2.54	2.45	−2.48	−0.25	25.12	0.02	0.02
Exp. D-0	0	7.26	0.02	1.01	1.06	0.52	−2.02	4.03	−0.90	−0.24	26.71		
Exp. D-1	62	6.75	0.17	0.84	1.04	0.86	−2.82	1.62	−3.31	−0.25	24.30	5.16	5.69
Exp. D-2	157	6.77	0.20	0.81	1.05	0.88	−2.76	1.78	−3.15	−0.25	24.45	0.62	0.56
Exp. D-3	1378	6.82	0.44	0.59	1.07	0.87	−2.67	2.08	−2.85	−0.24	24.75	0.54	0.50
Exp. D-4	3007	6.85	0.58	0.47	1.08	0.88	−2.61	2.28	−2.65	−0.23	24.95	0.29	0.27
Exp. D-5	5880	6.82	0.74	0.32	1.09	0.95	−2.63	2.21	−2.72	−0.23	24.89	0.30	0.28
Exp. D-6	8308	6.83	0.75	0.30	1.08	0.88	−2.65	2.16	−2.77	−0.23	24.83	0.06	0.07
Exp. D-7	10995	6.83	0.76	0.27	1.07	0.83	−2.67	2.08	−2.85	−0.24	24.76	0.05	0.06

* calculated as the average of similar values (^{28}Si and ^{29}Si) within the error.

[a] the values of total [Si] reported here are the combined sum of [^{28}Si], [^{29}Si], and [^{30}Si]. Values of [^{28}Si] and [^{29}Si] were determined through analytical measurements while [^{30}Si] was estimated based on natural isotopic abundance of Si, using a fixed ratio relative to [^{28}Si].

[b] based on greenaline solubility from Eugster and Chou (1973).

[c] for critical supersaturation of Fe(II)-silicate from Tosca et al. (2016).

$$\frac{d[^{29}Si]}{dt} = \frac{V_{Si,dis}.m.R_{dis}.\left(\frac{[^{29}Si]}{[Si]}\right)_{dis} - V_{Si,pre}.m.R_{pre}.\left(\frac{[^{29}Si]}{[Si]}\right)_{\bar{t}}}{M} \quad (3)$$

Rearranging Eqs. (2) and (3) gives:

$$\left(\frac{d[^{28}Si]}{d[Si]}\right)_{\bar{t}} = \frac{V_{Si,dis}.m.R_{dis}.\left(\frac{[^{28}Si]}{[Si]}\right)_{dis} - \frac{d[^{28}Si]}{dt}}{V_{Si,pre}.m.R_{pre}} \quad (4)$$

$$\left(\frac{d[^{29}Si]}{[Si]}\right)_{\bar{t}} = \frac{V_{Si,dis}.m.R_{dis}.\left(\frac{[^{29}Si]}{[Si]}\right)_{dis} - \frac{d[^{29}Si]}{dt}}{V_{Si,pre}.m.R_{pre}} \quad (5)$$

Then, R_{dis} can be obtained by solving Eqs. (4) and (5) together as:

$$R_{dis} = \frac{M}{V_{Si,dis}.m} \frac{\frac{d[^{28}Si]}{dt} - \frac{d[^{29}Si]}{dt}.\left(\frac{[^{28}Si]}{[^{29}Si]}\right)_{\bar{t}}}{\left(\frac{[^{28}Si]}{[Si]}\right)_{dis} - \left(\frac{[^{29}Si]}{[Si]}\right)_{dis}.\left(\frac{[^{28}Si]}{[^{29}Si]}\right)_{\bar{t}}} \quad (6)$$

by following the same procedure, R_{pre} can also be obtained as:

$$R_{pre} = \frac{M}{V_{Si,pre}.m} \frac{\frac{d[^{29}Si]}{dt} - \frac{d[^{28}Si]}{dt}\left(\frac{[^{29}Si]}{[^{28}Si]}\right)_{dis}}{\left(\frac{[^{28}Si]}{[Si]}\right)_{\bar{t}}.\left(\frac{[^{29}Si]}{[^{28}Si]}\right)_{dis} - \left(\frac{[^{29}Si]}{[Si]}\right)_{\bar{t}}} \quad (7)$$

With the subscript *dis* referring to the substrates with natural isotopic composition. The subscript $\bar{t}$ represents the middle time between two samples where the isotopic composition is changing between the mineral and the fluid (Che et al., 2021). All rates are reported in *mol/g/s*. This derivation does not consider the effect of the isotope fractionation on the rate calculations. Although isotope fractionation occurs during this process, it has only a negligible contribution to the uncertainty for the reaction rate determination (Che et al., 2021; Gruber et al., 2013; Zhu et al., 2016).

The error propagation methods presented by Rimstidt (2014) were used to estimate the propagated uncertainties for the reaction rate calculations. Each parameter in Equations (6) and (7) bears its own uncertainty therefore the resultant effect of each uncertainty was considered by using the following approach:

$$\delta f = \sqrt{\sum_i \left(\frac{\partial f}{\partial x_i}\right)^2 .(\delta x_i)^2} \quad (8)$$

where δf is the uncertainty on the calculated parameters and ∂x_i is the uncertainty of the measured subscripted element, i (^{28}Si, ^{29}Si etc.).

2.3. Analytical measurements

[Fe] and [Si] in samples from the Fe(II)-silicate precipitation experiment were analyzed using a Varian 725-ES Inductively Coupled Plasma Optical Emission Spectrometer (ICP-OES) at the University of Calgary. Prior to each analysis, the ICP-OES was calibrated ($R^2 > 0.999$) via serial dilution of certified Fe and Si standards (BDH Limited). Analytical precision and accuracy for these analyses are typically better than ± 5 %, and thus 5 % is used to calculate the uncertainty on fluid elemental concentrations discussed below.

Quantification of [^{28}Si] and [^{29}Si], as well as [Fe], for samples from each doping experiment were performed using a ThermoFisher iCAP™ Triple Quadrupole Inductively Coupled Plasma-Mass Spectrometer, (ICP-MS; Thermo Scientific, Bremen, Germany) coupled to an ESI SC-4 DX FAST (ESI) autosampler at the University of Calgary. The ICP-MS instrument was optimized in STD-mode in a daily routine using a tuning solution (Thermo Scientific) to obtain maximum signal intensity while maintaining high stability and low oxide and double-charged rates. The instrument was run in single-quadrupole kinetic energy discrimination mode (SQ-KED) using helium gas in the collision cell. General instrumental settings for Fe elemental analysis and the Si isotope quantification measurements are described in Table S1.

Prior to [^{29}Si] and [^{28}Si] quantification, samples were blank corrected using 2 % hydrochloric acid. The [^{29}Si] and [^{28}Si] quantification was accomplished by external calibration (6-point calibration, for [^{28}Si] ranging from 0.01 µg/mL to 1 µg/mL and for [^{29}Si] ranging from 0.01 µg/mL to 5 µg/mL). The ^{28}Si standards were prepared from a single-element stock solution (BDH Limited) in 2 % hydrochloric acid. The ^{29}Si standards were prepared from a ^{29}Si stock solution (from IsoFlex USA, San Francisco, California, see section 2.2) in 2 % hydrochloric acid. Furthermore, the performance of the ^{29}Si and ^{28}Si quantification was monitored with mixtures of ^{28}Si and ^{29}Si solutions (QCs) throughout the measurement. Precision of the QC values for the mixtures were 100 % ± 2 %. Total combined uncertainties for [^{29}Si] and [^{28}Si] quantification were estimated below 5 %. At the end, measured mass concentrations were converted into molal concentrations. The values of [Si] reported in Table 1 are the combined sum of [^{28}Si], [^{29}Si], and [^{30}Si]. Values of [^{28}Si] and [^{29}Si] were determined through analytical measurements while [^{30}Si] was estimated based on natural isotopic abundance of Si.

For Fe mass concentration analysis of doping solutions, an aliquot of each leaching step was diluted by a factor of 10 with 2 % nitric acid. The Fe quantification was accomplished by external calibration (8-point calibration, for Fe ranging from 1 µg/L to 1500 µg/L) with standards prepared volumetrically from multi-element stock solution (BDH89800-580, Aristar, VWR International) including 2 µg/L indium (In) as an internal normalization standard. The relative expanded uncertainties for Fe mass concentration analysis were estimated as 5 %. At the end, measured mass concentrations were converted into molal concentrations.

2.4. FT-IR and SEM-EDS analysis

Fourier Transform Infrared (FT-IR) spectroscopy was performed by using Thermo Nicolet 4700 FT-IR spectrometer in transmission mode over the wavenumber range of 400 cm^{-1} to 4000 cm^{-1} by mixing the dry Fe(II)-silicate (for solids before and after the Si doping experiments) with KBr powder. The solid mixtures were prepared in the anerobic chamber and converted immediately into pellets via pellet press. Each FT-IR measurement took less than a minute. A Thermo Scientific Phenom G6 Pro scanning electron microscope (SEM) with a coupled Energy Dispersive Spectroscopy (EDS) system was used to chemically analyze the Fe(II)-silicate during the experiment. The major benefit of SEM-EDS to our study is that it can help to evaluate the compositional variations (e. g., Fe/Si ratio) of precipitates in situ. Data for FT-IR and EDS analysis is provided in the Supplementary Material.

2.5. Geochemical calculations

The Geochemist's Workbench (GWB) software package (Bethke et al., 2022) employing a custom thermodynamic database generated by using the PyGeochemCalc (PyGCC) (Awolayo and Tutolo, 2022) was used to calculate ion activities and mineral saturation states. Estimated log(K) value for crystalline greenalite was sourced from Eugster and Chou (1973) and additionally calculated using PyGCC with the Blanc et al. (2015, 2021) model, which builds on earlier estimates by Miyano and Klein (1983). The equilibrium constant for critical supersaturation of Fe(II)-silicate incorporated into the database was taken from Tosca et al. (2016). The composition of the measured solution was used to calculate the ion activity product (Q) of Fe(II)-silicate as follows

$$Q = \frac{a^3_{Fe^{2+}} a^2_{SiO_2}}{a^6_{H^+}} \quad (9)$$

where a is the activity of subscripted aqueous species.

2.6. Stokes' Settling Velocity calculation

We also calculated Stokes' settling velocity of greenalite nanoparticles based on the following formulation (Lerman et al., 1974):

$$U = \frac{g(d_p - d_m)D^2}{18\nu} \quad (10)$$

where U is the settling velocity (m/s), g is the gravitational acceleration (9.8 m/s^2), D is the particle diameter (m), d_p is the particle density (kg/m^3), d_m is the density of the medium (kg/m^3), and ν is the viscosity (kg/m/s).

3. Results

3.1. Precipitation of Fe(II)-silicate

ICP-OES analyses of samples acquired throughout the precipitation experiment show a consistent decrease in Fe concentration whereas Si concentration increases slightly then plateaus (Fig. 1a). The resultant concentration changes are attributed to both the precipitation of Fe(II)-silicate and mixing of Fe^{2+} and Si solutions. Initially, pH rose steadily as the acidic Fe solution was titrated with the alkaline SiO_2 counterpart, though no precipitation occurred until the pH reached to ~ 7.5 (Fig. 1a). Tosca et al. (2016) demonstrated that a critical supersaturation (log (K_{crit}) = 27.6) must be achieved to trigger homogeneous nucleation of Fe(II)-silicate directly from the solution. Once this condition was met, the pH stabilized at approximately 7.6 (Fig. 1a), indicating that the continuous pH increase from titration was balanced by H^+ released during Fe(II)-silicate precipitation, as described by the reaction:

$$2\ SiO_{2(aq)} + 3\ Fe^{2+} + 5\ H_2O \leftrightarrow Fe_3^{2+}Si_2O_5(OH)_4\ (\text{greenalite}) + 6H^+ \quad (R1)$$

The Fe and Si stoichiometry in the precipitated solids was determined by tracking changes in solution chemistry over time (Fig. 1b). The average Fe/Si ratio in the solid phase remained relatively constant throughout the experiment at an average value of 1.15 (Fig. 2). While slightly lower than the Fe/Si ratio of crystalline greenalite (1.5, see Reaction (1)), this value aligns well with the characteristics of hydrated, poorly crystalline Fe(II)-silicate (Tosca et al., 2016; Tostevin and Sevgen, 2024). SEM-EDS spot analysis confirmed similar Fe/Si trends in the precipitates (Fig. 2). The precipitation of amorphous SiO_2 (SiO_2(am)) and Fe-brucite ($Fe(OH)_2$) along with Fe(II)-silicate during the experiment was unlikely as the solution chemistry remained undersaturated with respect to these phases (Fig. 3). FT-IR analyses of the precipitated product revealed distinct IR peaks at 461 cm^{-1} (Fe^{2+}—O stretch), 658 cm^{-1} (Fe_3^{2+}—OH bend), 1017 cm^{-1} (Si—O stretch), 1626 cm^{-1} and 3400 cm^{-1} (surface-adsorbed H_2O), and 3625 cm^{-1} (Fe_3^{2+}—OH stretch) (Fig. 4). These results are consistent with the characteristic FT-IR peaks for greenalite (Stubican and Roy, 1961; Tosca et al., 2016; Jiang and Tosca, 2019; Tostevin and Sevgen, 2024).

3.2. Si doping experiments

Four sets of Si isotope doping experiments (Exp. I, Exp. H, Exp. Q, Exp. D) were conducted to assess the effect of saturation state on the reactivity of Fe(II)-silicate (Table 1). Blank experiments, using the same solutions without the solid, were also performed as a control. All samples collected during the experiments remained below the critical supersaturation for Fe(II)-silicate and thus no significant changes in solution chemistry due to homogeneous nucleation of Fe(II)-silicate were expected (Fig. 3). Results from all experiments showed a sharp decrease in [^{29}Si] and an increase in [^{28}Si] over time, with the relative proportions of these changes revealing three distinct patterns (Fig. 5). Based on these changes, the forward (R_{pre}) and the reverse (R_{dis}) reaction rates for Reaction (1) were calculated for each experiment using Equations (6) and (7), respectively. In Exp. I, the removal rate of ^{29}Si was faster than the release of ^{28}Si, leading to a depletion of [Si] over time (Fig. 5) and indicating early dominance of precipitation over dissolution in the reaction regime (Fig. 6). In contrast, Exp. H exhibited the opposite trend, resulting in an accumulation of total Si in the fluid (Fig. 5) and indicating that dissolution rate was faster than the precipitation rate (Fig. 6). In both Exp. I and Exp. H, as the systems approached steady-state conditions, the forward and reverse reaction rates converged (Fig. 6). Exp. Q and Exp. D, on the other hand, displayed similar behavior, with the rates of change for each Si isotope behaving similarly. As a result, there was no change in [Si] over time in either experiment (Fig. 5), in turn indicating that R_{pre} and R_{dis} were approximately equal during these experiments (Fig. 6).

When the doping solution came into contact with the Fe(II)-silicate in the reactors, Fe concentration increased, and pH decreased in all four experiments after about an hour. However, both parameters remained relatively constant for the remainder of the experiments

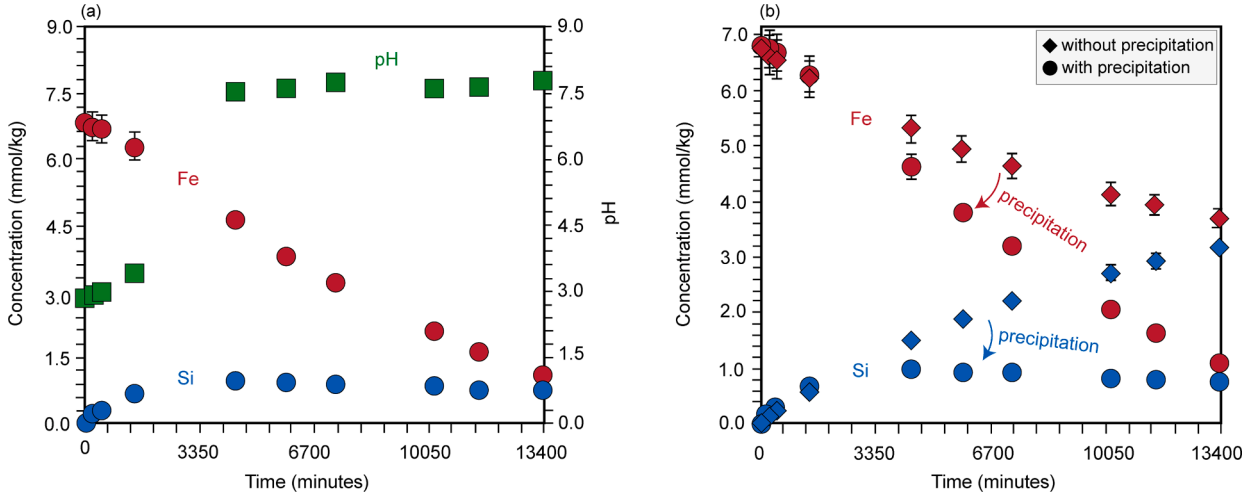

Fig. 1. Results of the Fe(II)-silicate precipitation experiment. (a) Changes in pH, Fe, and Si concentrations over time. (b) Calculation of precipitated fraction based on fluid chemistry. The upper data points for Fe and Si represent fluid evolution without precipitation (or only dilution), while the lower data points are the analytical measurements reflecting the combined effects of precipitation and dilution. The precipitated fraction is calculated by using the difference between Fe and Si concentration in each data point. Error bars are shown for all data points but are smaller than the symbols where applicable.

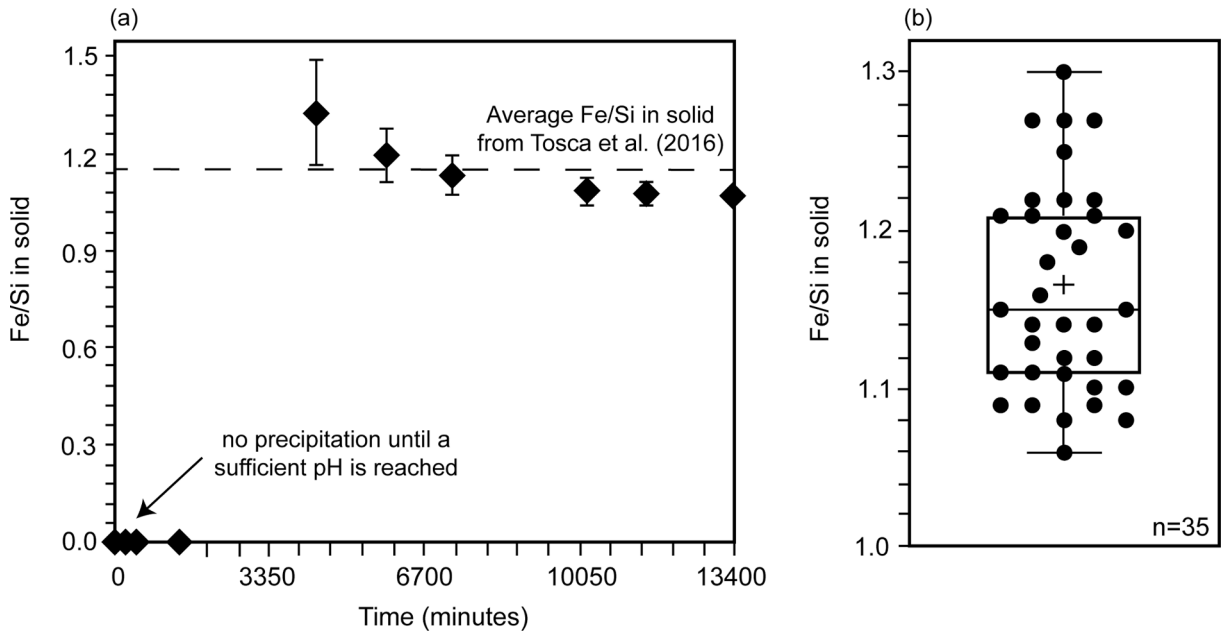

Fig. 2. The Fe/Si ratio in the precipitated solid, (a) determined from fluid chemistry, and (b) from SEM-EDS analysis, remains relatively constant throughout the experiment, with an average value of 1.15 (dashed line in (a) and + in (b)), consistent with Tosca et al. (2016). Error bars are shown for all data points but are smaller than the symbols where applicable.

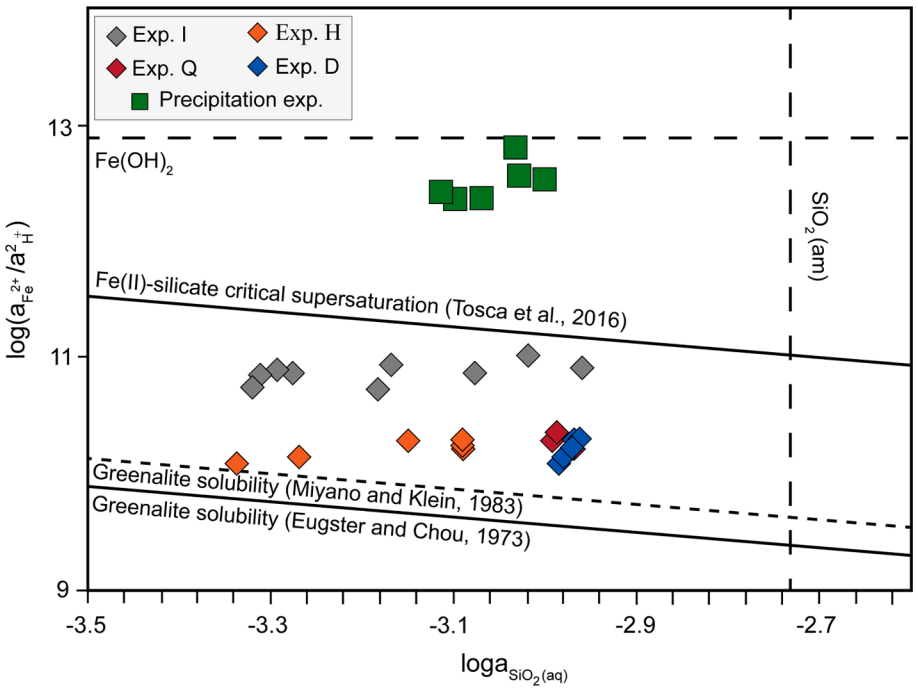

Fig. 3. Activity-activity diagram for the Fe-SiO_2 system at 25 °C. The upper solid line represents the critical supersaturation boundary for Fe(II)-silicate (adapted from Tosca et al., 2016), while the lower solid (Eugster and Chou, 1973) and dashed (Miyano and Klein, 1983) lines correspond to the solubility of crystalline greenalite. The solution compositions from each experiment are plotted in different colors. The precipitation experiment (green squares) started with an initial fluid composition above the Fe(II)-silicate critical supersaturation boundary, allowing homogeneous nucleation to occur. The saturation states of the solutions used in the silicon isotope doping experiments lie between the solubility of greenalite and its critical supersaturation threshold. Solubility boundaries for amorphous SiO_2 (Siever, 1962) and Fe-brucite (Feitknecht and Schindler, 1963) are also included for reference.

(Fig. S2). On the other hand, no variation in [Fe] or [Si] was observed in blank experiments (Fig. S2), which indicates that Fe(II)-silicate plays a key role in controlling the evolution of the solution chemistry. Finally, FT-IR data for the post-experiment solids collected from each experiment showed no observable change in the Fe(II)-silicate after the doping experiments (Fig. 4).

4. Discussion

4.1. Interplay of thermodynamics and kinetics of Fe(II)-silicate reactions at near-equilibrium conditions

Investigating near-equilibrium kinetics using Si isotope doping permits evaluation of the solubility of Fe(II)-silicate, as near-equilibrium

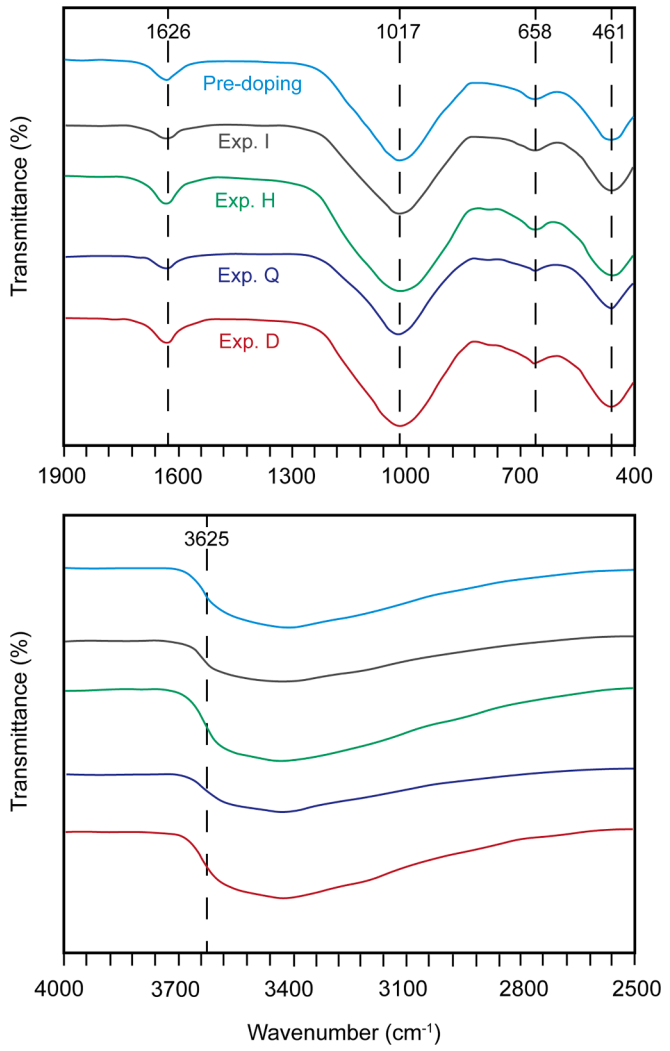

Fig. 4. Fourier Transform Infrared (FT-IR) spectroscopy results for Fe(II)-silicate before and after the silicon isotope doping experiments. Fe(II)-silicate revealed distinct IR peaks at 461 cm^{-1} (Fe^{2+}-O stretch), 658 cm^{-1} (Fe_3^{2+}–OH bend), 1017 cm^{-1} (Si-O stretch), 1626 and 3400 cm^{-1} (surface-adsorbed H_2O), and 3625 cm^{-1} (Fe_3^{2+}–OH stretch), consistent with IR peaks of greenalite (see text).

conditions highlight the interplay between kinetics and thermodynamics. According to the Principle of Detailed Balance (PDB), as a system approaches thermodynamic equilibrium, the forward and reverse reaction rates converge and eventually become equal at equilibrium (see *e. g.,* Rimstidt, 2014; Che et al., 2021; Liu et al., 2016). Typically, steady state fluid chemistry measurements are interpreted as the apparent solubility of the amorphous phase (Tosca et al., 2011; Tutolo and Tosca, 2018). Che et al. (2021) showed that the concept of apparent solubility for amorphous Mg-silicate suggests a metastable equilibrium between the amorphous phase and the surrounding fluid. Our findings align with this metastable equilibrium approach, as the dissolution and precipitation rates of Fe(II)-silicate become nearly equal as saturation approaches apparent solubility (Fig. 6). However, the evolution of solution chemistries towards saturation states of Exp. Q and Exp. D (Fig. 7) and the relatively constant precipitation and dissolution rates during each of these experiments (Fig. 6) suggest the need for a more precise definition beyond quasi-equilibrium for this Fe(II)-silicate system. Therefore, we calculated ion activity product (Q) values for each data point in Fig. 7 according to the dissolution reaction of greenalite based on Equation (9).

Equation (9) assumes ideal greenalite stoichiometry (see Reaction (1)) although precursor Fe(II)-silicate phase has slightly lower Fe/Si ratio (Fig. 2). This ratio in the solids is lower perhaps due to the SiO_2 sorption onto the precursor phase (Tostevin and Sevgen, 2024). Then, following Nagy et al. (1991), we averaged the ion activity product (Q) values using data points representing the slowest rates from Exp. Q and Exp. D, which are representative of steady state condition. This calculation yields a solubility product for Fe(II)-silicate of $\log(K) = 24.9 \pm 0.25$ (Fig. 7). This value is several orders of magnitude lower than the threshold for homogeneous nucleation of Fe(II)-silicate ($\log(K) = 27.6$, Tosca et al., 2016). A similar trend is observed in the Mg-silicate system (Arizaleta et al., 2020; Tutolo and Tosca, 2018), as homogeneous nucleation directly from a solution requires more energy than growth on a pre-existing surface (Stumm, 1992). Solubility of crystalline greenalite estimations by Eugster and Chou (1973) and Miyano and Klein (1983) are several orders of magnitude lower than our solubility calculation for Fe(II)-silicate (Fig. 7). This indicates that Fe(II)-silicate is more soluble than crystalline greenalite under given geochemical conditions. This is consistent with the trends observed in the Mg-silicate system, where experiments have shown that crystalline Mg-silicates are far less reactive than their amorphous counterparts (Che et al., 2021).

4.2. *Geological implications*

Accurately determining the true nature of primary precipitates in BIFs is crucial for understanding the dissolved Fe^{2+} concentration and pH of Archean oceans. Since BIFs are chemical sedimentary rocks, the solubility of the primary precipitates should control such proxies in the Archean water column (Tosca et al., 2019). While previous studies have proposed various potential mineralogical sinks for Fe and SiO_2 such as Fe(III)-oxyhydroxides or green rust (Fischer and Knoll, 2009; Halevy et al., 2017; Konhauser et al., 2017; Johnson et al., 2022a), a wealth of geological evidence supports the idea that greenalite nanoparticles were among the precursor minerals for BIFs (Johnson et al., 2018; Rasmussen et al., 2015, 2021; Rasmussen et al., 2022; Rasmussen et al., 2024a; Rasmussen and Muhling, 2021). The SiO_2 concentration in the deep Archean water column was most likely limited by the solubility of SiO_2(am) prior to the emergence of silicifying organisms (Maliva et al., 2005; Siever, 1992; Conley et al., 2017). Jiang and Tosca (2019) experimentally demonstrated that Fe(II)-silicate could have served as the solubility-limiting phase controlling Fe^{2+} concentrations in Archean waters, even under conditions of significant supersaturation with respect to amorphous Fe(II)-carbonates.

Tosca et al. (2016) highlighted the strong influence of pH on Fe(II)-silicate nucleation kinetics, with homogenous nucleation being far less effective below pH 7.25 (Rasmussen et al., 2023). This pH constraint leaves only a narrow window for greenalite nucleation directly from seawater at 25 °C, as estimates of Archean seawater pH range around ~ 6.0–7.5 (Halevy and Bachan, 2017; Krissansen-Totton et al., 2018). However, reaction path modelling results suggest that mixing of Archean seawater with hydrothermal fluids could initiate greenalite precipitation in the vent plumes (Tosca and Tutolo, 2023). Moreover, the rare earth element and yttrium (REY) trends in greenalite indicate that it may have also precipitated directly from seawater in a shelf environment, controlled by a combination of physicochemical conditions (Nke et al., 2024). However, regardless of the source of formation, greenalite nanoparticles would need to be stable enough to remain in the water column, transport and settle as a precursor mineral forming BIFs (Rasmussen et al., 2021). Our Fe(II)-silicate solubility calculations suggest that, once nucleated, Fe(II)-silicate could remain in the water column at Fe^{2+} concentrations an order of magnitude lower than those needed for homogenous nucleation of greenalite (Jiang and Tosca, 2019) within a relevant pH range for Archean ocean waters (Fig. 8). Moreover, Che et al. (2021) showed that increasing crystallinity decreases reactivity at near-equilibrium conditions. Therefore, if hydrothermally sourced greenalite had higher crystallinity than Fe(II)-silicate

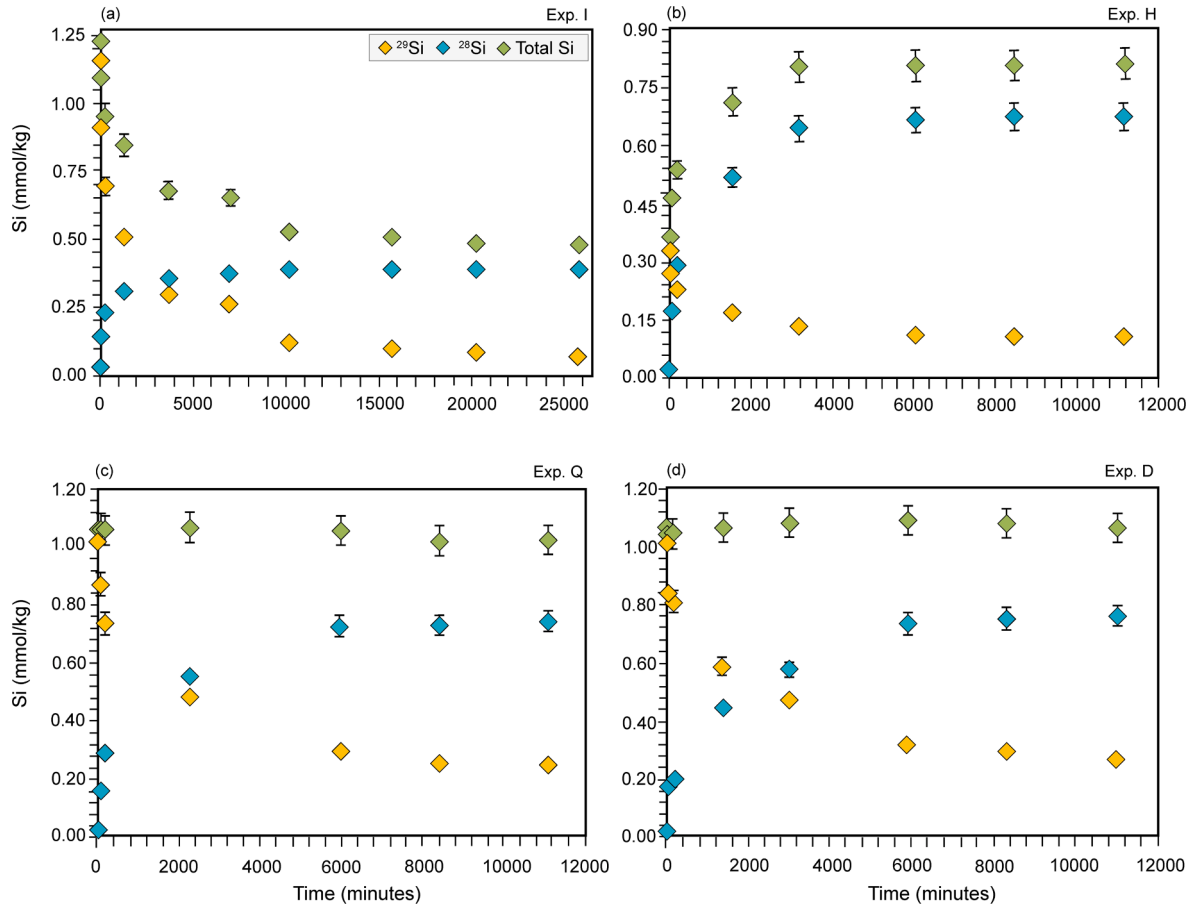

Fig. 5. Fluid chemistry results from the silicon doping experiments for Exp. I (a), Exp. H (b), Exp. Q (c), and Exp. D (d). The concentration changes of ^{28}Si, ^{29}Si, and total Si over time are presented in each plot. Total Si is calculated as [^{28}Si] + [^{29}Si] + [^{30}Si], where [^{30}Si] is determined based on the natural isotopic abundance of silicon. Error bars are shown for all data points but are smaller than the symbols where applicable.

(Rasmussen et al., 2024b), thermodynamic constraints would suggest its stability at even lower Fe^{2+} concentrations (Fig. 8).

Mineral assemblages in BIFs are closely associated with chert as observed in various studies (Bekker et al., 2013; Konhauser et al., 2017; Maliva et al., 2005; Rasmussen et al., 2021; Rasmussen and Muhling, 2021). To explain this phenomenon, Rasmussen and Muhling (2021) proposed a mechanism based on the greenalite precipitation model to account for the interplay between the Fe and silica cycles in Archean ocean system. They proposed that, after nucleation of greenalite, a 'greenalite-silica shuttle' facilitates silica sorption onto greenalite nanoparticles and their co-transportation to the seafloor. This process was suggested earlier for Fe oxyhydroxides (Fischer and Knoll, 2009). Moreover, the observed Si sorption trend is similar with what has been observed for other comparable phyllosilicates (Siever, 1992; Tutolo and Tosca, 2018). Indeed, Tostevin and Sevgen (2024) showed that silica sorption on Fe(II)-silicate is an effective process in a plausible Archean ocean water composition, and that, once deposited, excess silica could be released into sediment pore waters at elevated temperatures during early diagenesis and eventually could form chert layers through compaction (cf. Rasmussen et al., 2021). A similar trend is evident in our experimental results, resulting in overall total Si drawdown in the solution (Fig. 5a). This process is the most effective when the system is above the solubility limit of Fe(II)-silicate (*i.e.,* $\log(K) = 24.9 \pm 0.25$). Therefore, our results provide a mechanistic understanding of why greenalite is remarkably preserved as nanoparticles trapped in chert of Archean age. This preservation is attributed to the relatively low reactivity of greenalite and its ability to co-deposit with silica, forming and embedding within chert layers (Rasmussen et al., 2021).

BIFs were deposited in settings ranging from basin floors to shelves (Bekker et al., 2013; Beukes, 1984; Beukes and Klein, 1990; Klein, 2005; Krapež et al., 2003; Pufahl et al., 2014; Rasmussen et al., 2017, 2021; Rasmussen and Muhling, 2021; Trendall, 2002), indicating that greenalite nanoparticles may have needed to have been transported hundreds to thousands of kilometers from vent sources to the locus of BIF deposition. Modern-day studies in the East Pacific Rise have shown that hydrothermal Fe can be transported over 4000 km in deep ocean basins (Resing et al., 2015; Fitzsimmons et al., 2017, Moffett and German, 2018), a portion of this transport likely occurring as Fe-bearing nanoparticles (Findlay et al., 2019; Gartman et al., 2019; Yücel et al., 2011; Yücel et al., 2021). For the "greenalite-silica shuttle" to function effectively, greenalite nanoparticles must be stable enough to withstand complex dissolution and sorption processes during long-distance transport. The near-equilibrium reaction rate calculations from our experiments indicate that the precipitation reaction (*i.e.,* R_{pre}) dominates the reaction regime at conditions above Fe(II)-silicate saturation.

We calculated Stokes' settling velocity of greenalite nanoparticles based on Equation (10). In this calculation, we used 0.00096 kg/m/s for the viscosity of seawater at 25 °C and 1023 kg/m^3 for the density of seawater at 25 °C (Sharqawy et al., 2010; Nayar et al., 2016). The average density of a greenalite particle is approximately 3000 kg/m^3 (Gruner, 1936). Our calculation is based on a particle size of 200 nm, an average size of greenalite nanoparticles consistent with high-resolution transmission electron microscopy images from greenalite-rich chert layers in BIFs (Rasmussen et al., 2015; Rasmussen et al., 2017). This size is also similar to pyrite nanoparticles found in modern-day hydrothermal vents (Yücel et al., 2011). We calculated the Stokes' settling velocity of greenalite nanoparticles to be approximately 1.4 m/year. In this calculation, we assumed the settling of spherical particles under laminar

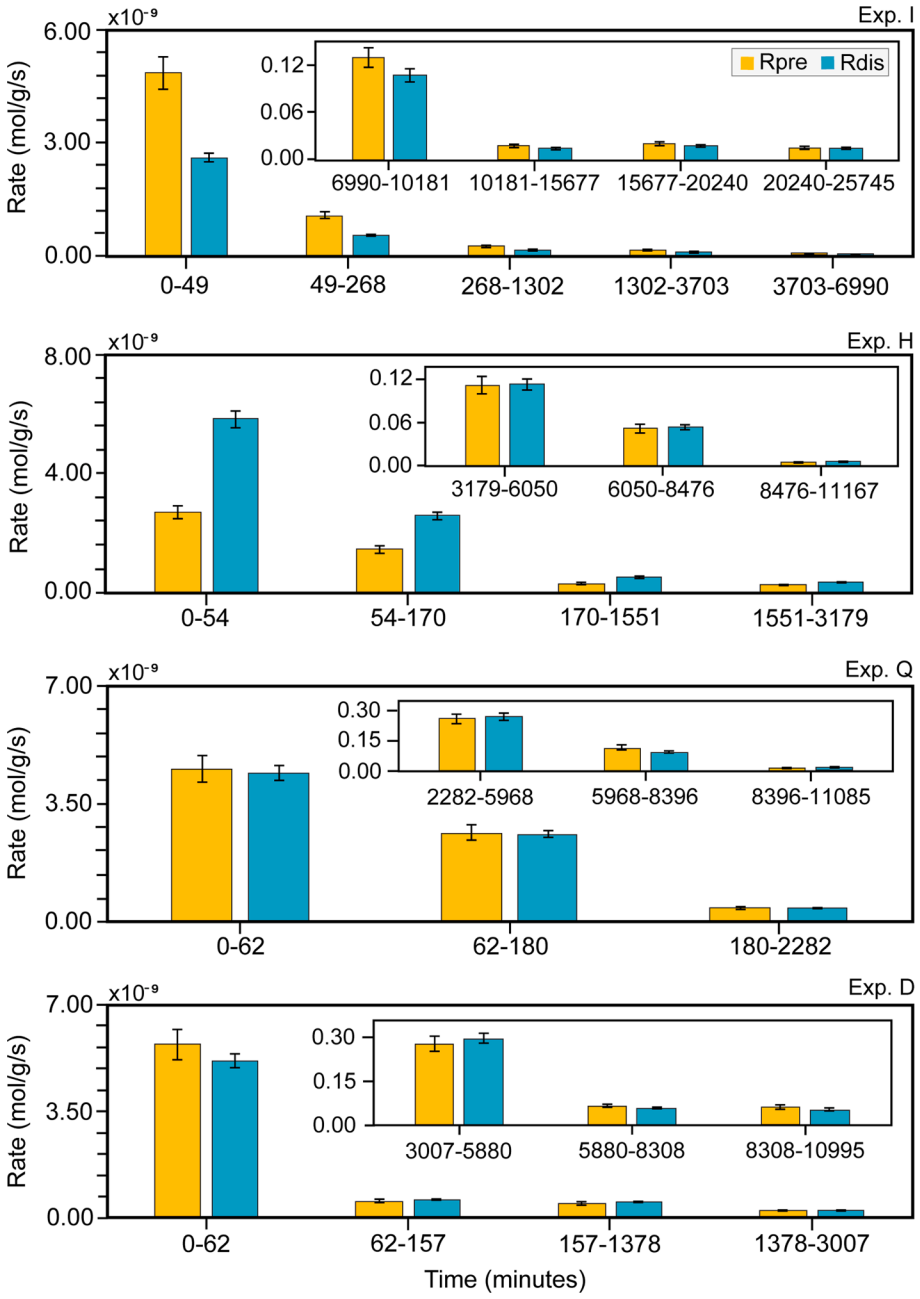

Fig. 6. Dissolution (R_{dis}) and precipitation (R_{pre}) rates for Exp. I (a), Exp. H (b), Exp. Q (c), and Exp. D (d), calculated based on the concentration changes of ^{28}Si and ^{29}Si over time. Error bars are shown for all data points but are smaller than the bars where applicable.

flow. However, the platy nature of greenalite nanoparticles (Rasmussen et al., 2015; Rasmussen et al., 2017), which have larger surface area-to-volume ratios, and the contribution of ocean water mixing, would likely slow the settling velocity even further. Additionally, pyrite, with a particle density of approximately 5000 kg/m^3 (Yücel et al., 2021), is significantly denser than greenalite. As a result, under identical water column physical conditions, greenalite would remain suspended for nearly twice as long as pyrite (Tosca and Tutolo, 2023).

Silica sorption onto Fe(II)-silicate is possible, as observed in our experimental system (e.g., Exp. I). Following sorption, the accumulated amorphous silica can polymerize over time, as indicated in Tostevin and Sevgen (2024). This phenomenon, along with the aggregation of greenalite particles (Rasmussen et al., 2019b), could influence both the particle diameter and density, thereby affecting the settling velocity calculations. However, it is important to note that, while particle aggregation may increase the effective particle diameter, it can simultaneously decrease the overall density due to the incorporation of interstitial water within the newly formed, higher-porosity aggregate structure. This interplay between aggregation, density and particle size underscores the complexity of accurately modeling particle settling velocities.

To gain further insights into this phenomenon and to better understand hydrothermal particle transport in the water column, observational data from present-day oceanic settings would be invaluable. Fitzsimmons et al. (2017) examined the distribution of hydrothermal Fe in both particulate and dissolved forms over a distance of 4000 km from the vent source at the Southern East Pacific Rise (SEPR), taking into account the aggregative settling of particles. As they showed, not all hydrothermal Fe transforms into particulate form upon emission from the vent orifice (see also Findlay et al., 2015 and Yücel et al., 2021). A

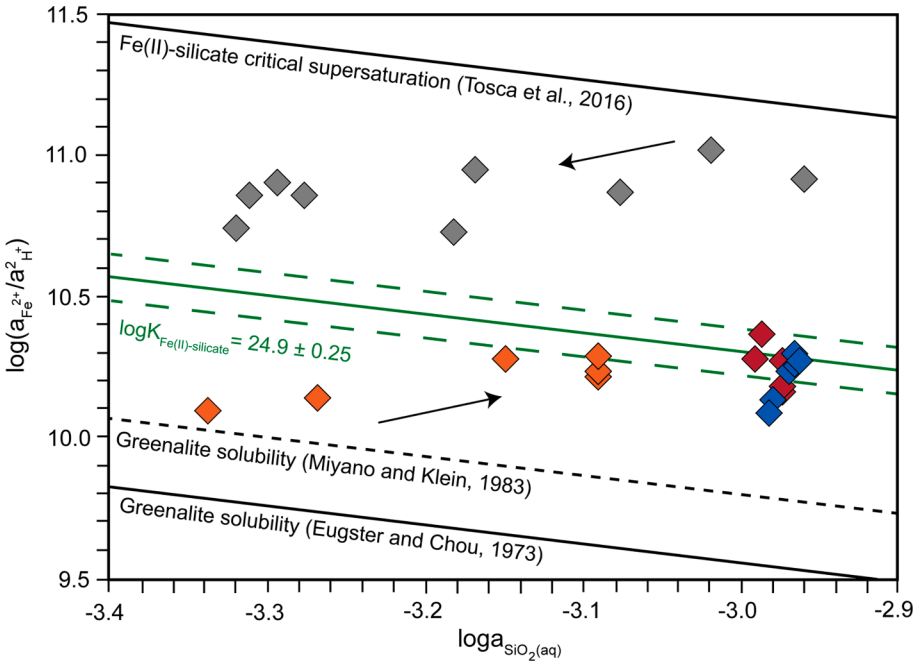

Fig. 7. Activity-activity diagram for the Fe-SiO_2 system at 25 °C (see also Fig. 3). Arrows indicate the direction of chemical evolution for Exp. I and Exp. H. A new solubility product for Fe(II)-silicate is determined based on the data points corresponding to the slowest reaction rates in Exp. Q and Exp. D (see text for details). The green solid line is for the calculated log(K) value for Fe(II)-silicate, with the dashed lines showing the 95 % confidence interval. Log(K) values for critical supersaturation of Fe(II)-silicate (Tosca et al., 2016), and for crystalline greenalite (Eugster and Chou, 1973; Miyano and Klein, 1983) are also shown. The legend is the same as in Fig. 3.

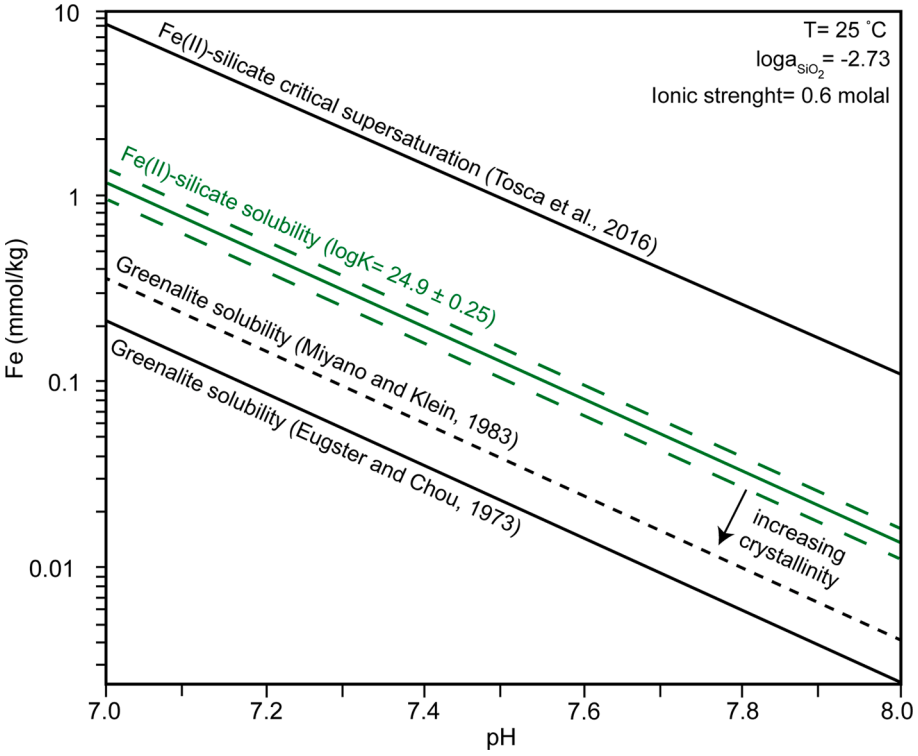

Fig. 8. Maximum Fe^{2+} concentration as a function of pH, calculated using the newly determined solubility of Fe(II)-silicate (green solid line), with 95 % confidence intervals (green dashed lines). The system is set to amorphous SiO_2 saturation (see text), and the ionic strength is based on Archean seawater composition adapted from Tosca and Tutolo (2023). The Fe^{2+} concentration required to initiate homogeneous Fe(II)-silicate nucleation is also shown (upper black line) (Tosca et al., 2016). As crystallinity increases from amorphous Fe(II)-silicate to crystalline greenalite, precipitated solid phase is stable at lower Fe^{2+} concentrations for a given pH.

portion remains as dissolved Fe and can be traced up to 4000 km away from the vent source (Resing et al., 2015). In addition, while particulate Fe experiences aggregative removal upon mixing, it can still persist in the water column and be transported further away from the vent source (Fitzsimmons et al., 2017).

Therefore, our results indicate that, just as hydrothermal Fe is transported across long distances in the modern deep ocean (Resing et al., 2015; Fitzsimmons et al., 2017), the transport of greenalite nanoparticles from deep-ocean hydrothermal vent sources to BIF deposition sites, incorporating silica along the way and creating the "greenalite-silica shuttle", is plausible in the Archean ocean system with lower Fe^{2+} concentrations than previously estimated. In conjunction with the observed silica sorption behavior with the persistent background silica flux that is characteristic of the unique depositional styles of Archean chert, these findings point towards a dynamic process that likely played a critical role in the formation of BIFs. Specifically, the periodic waxing and waning of greenalite nanoparticle transport into BIF depositional environments as a function of variations in hydrothermal flux or evolving ocean currents emerges as a plausible mechanism to account for the alternating Fe- and Si-enriched layers that are preserved within BIFs (Rasmussen et al., 2017; Rasmussen and Muhling, 2021).

5. Conclusion

Numerous minerals, and accompanying precipitation processes, have been proposed to explain the source of Fe in BIF deposits. While decades of work have suggested Fe-oxyhydroxides and green rust form primary BIF precipitates, recent studies have identified greenalite as another potential alternative. In this study, we investigated the near-equilibrium kinetics of hydrated, amorphous Fe(II)-silicate, a precursor phase to crystalline greenalite. Si isotope doping experiments demonstrated that the reactivity of Fe(II)-silicate is closely linked to saturation state of the solution. Our kinetic analysis revealed that, as the system approaches equilibrium, forward and reverse reaction rates converge. By integrating kinetic and thermodynamic data, we established a new solubility product for amorphous Fe(II)-silicate, $\log(K) = 24.9 \pm 0.25$. This indicates that Fe(II)-silicate is more soluble than crystalline greenalite but remains stable at lower Fe^{2+} concentrations than those required for nucleation of the amorphous phase directly from seawater. Evaluation of these findings indicates that, once formed, Fe(II)-silicate could persist in Archean ocean waters with Fe^{2+} concentrations as low as 1 mmol/kg and 10 μmol/kg at pH 7 and 8, respectively. Furthermore, at supersaturated conditions, silica would have sorbed onto Fe(II)-silicate. This sorbed silica could have been transported with Fe(II)-silicate through the deep ocean due to its slow settling velocity, and, upon deposition, released during early diagenesis, contributing to chert formation in Archean BIFs.

CRediT authorship contribution statement

Serhat Sevgen: Writing – original draft, Visualization, Methodology, Investigation, Formal analysis, Data curation, Conceptualization. **Anika Retzmann:** Writing – review & editing, Methodology, Investigation, Data curation. **Michael Nightingale:** Methodology, Investigation, Data curation. **Juan Carlos de Obeso:** Writing – review & editing, Methodology. **Qin Zhang:** Writing – review & editing, Methodology. **Ian Fleming:** Methodology. **Rosalie Tostevin:** Writing – review & editing. **Nicholas J. Tosca:** Writing – review & editing. **Benjamin M. Tutolo:** Writing – review & editing, Validation, Supervision, Software, Resources, Project administration, Methodology, Investigation, Funding acquisition, Conceptualization.

Data availability

The experimental data, and the Python code for calculating reaction rates can be accessed through Zenodo at https://doi.org/10.5281/zenodo.14847262.

Declaration of competing interest

The authors declare that they have no known competing financial interests or personal relationships that could have appeared to influence the work reported in this paper.

Acknowledgements

This research was funded by the Natural Sciences and Engineering Research Council of Canada under Discovery Grant RGPIN-2023-03361 (BMT). We thank Sılanur Sevgen for helping the figure designs. The authors also thank Jeffrey Catalano and the anonymous peer reviewers for their constructive criticism on this manuscript.

Appendix A. Supplementary material

Supplementary material to this article can be found online at https://doi.org/10.1016/j.gca.2025.02.015. The Supplementary Material includes a PDF file with a conceptual figure illustrating the experimental methodology, a table detailing analytical measurements, and plots showing changes in dissolved Fe and pH over time for each experiment, along with data from blank experiments.

References

Arizaleta, M.L., Nightingale, M., Tutolo, B.M., 2020. A rate law for sepiolite growth at ambient temperatures and its implications for early lacustrine diagenesis. Geochim. Cosmochim. Acta 288, 301–315.
Awolayo, A.N., Tutolo, B.M., 2022. PyGeochemCalc: a Python package for geochemical thermodynamic calculations from ambient to deep Earth conditions. Chem. Geol. 606.
Blanc, P., Vieillard, P., Gailhanou, H., Gaboreau, S., Gaucher, E., Fialips, C.I., Madé, B., Giffaut, E., 2015. A generalized model for predicting the thermodynamic properties of clay minerals. Am. J. Sci. 315, 734–780.
Blanc, P., Gherardi, F., Vieillard, P., Marty, N., Gailhanou, H., Gaboreau, S., Letat, B., Geloni, C., Gaucher, E., Made, B., 2021. Thermodynamics for clay minerals: calculation tools and application to the case of illite/smectite interstratified minerals. Appl. Geochem. 130, 104986.
Bekker, A., Planavsky, N.J., Krapež, B., Rasmussen, B., Hofmann, A., Slack, J.F., Rouxel, O.J., Konhauser, K.O., 2013. Iron Formations: Their Origins and Implications for Ancient Seawater Chemistry. in Treatise on Geochemistry Vol. 9, 561–628.
Beukes, N.J., 1984. Sedimentology of the kuruman and griquatown iron-formations, transvaal supergroup, Griqualand west, South Africa. Precambr. Res. 24, 47–84.
Beukes, N.J., Klein, C., 1990. Geochemistry and sedimentology of a facies transition from microbanded to granular iron-formation in the early Proterozoic Transvaal Supergroup, South Africa. In Precambrian Research 47.
Butler, I.B., Schoonen, M.A.A., Rickard, D.T., 1994. Removal of dissolved oxygen from water: a comparison of four common techniques. In Pergamon Talanta 41 (2).
Che, Z., Nightingale, M., Tutolo, B.M., 2021. Probing the application of kinetic theory to Mg-phyllosilicate growth with Si isotope doping. Geochim. Cosmochim. Acta 310, 205–220.
Conley, D.J., Frings, P.J., Fontorbe, G., Clymans, W., Stadmark, J., Hendry, K.R., Marron, A.O., De La Rocha, C.L., 2017. Biosilicification drives a decline of dissolved Si in the oceans through geologic time. Front. Mar. Sci. 4, 397.
Crowe, S.A., Paris, G., Katsev, S., Jones, C., Kin, S., Zerkle, A., Nomosatryo, S., Fowle, D. A., Adkins, J.F., Sessions, A.L., Farquhar, J., Canfield, D.E., 2014. Sulfate was a trace constituent of Archean seawater. Science 346 (6210), 735–739.
Findlay, A.J., Estes, E.R., Gartman, A., Yücel, M., Kamyshny, A., Luther, G.W., 2019. Iron and sulfide nanoparticle formation and transport in nascent hydrothermal vent plumes. Nat. Commun. 10 (1).
Fischer, W.W., Knoll, A.H., 2009. An iron shuttle for deepwater silica in late Archean and early Paleoproterozoic iron formation. Bull. Geol. Soc. Am. 121 (1–2), 222–235.
Fitzsimmons, J.N., John, S.G., Marsay, C.M., Hoffman, C.L., Nicholas, S.L., Toner, B.M., German, C.R., Sherrell, R.M., 2017. Iron persistence in a distal hydrothermal plume supported by dissolved-particulate exchange. Nat. Geosci. 10 (3), 195–201.
Gartman, A., Findlay, A.J., Hannington, M., Garbe-Schönberg, D., Jamieson, J.W., Kwasnitschka, T., 2019. The role of nanoparticles in mediating element deposition and transport at hydrothermal vents. Geochim. Cosmochim. Acta 261, 113–131.
Gong, L., Rimstidt, J.D., Zhang, Y., Chen, K., Zhu, C., 2019. Unidirectional kaolinite dissolution rates at near-equilibrium and near-neutral pH conditions. Appl. Clay Sci. 182.

Gruber, C., Harpaz, L., Zhu, C., Bullen, T.D., Ganor, J., 2013. A new approach for measuring dissolution rates of silicate minerals by using silicon isotopes. Geochim. Cosmochim. Acta 104, 261–280.
Gruner, J.W., 1936. The structure and chemical composition of greenalite. The American Mineralogist 21, 449–455.
Halevy, I., Alesker, M., Schuster, E.M., Popovitz-Biro, R., Feldman, Y., 2017. A key role for green rust in the Precambrian oceans and the genesis of iron formations. Nat. Geosci. 10 (2), 135–139.
Halevy, I., Bachan, A., 2017. The geologic history of seawater pH. Science 355 (6329), 1069–1071.
Hinz, I.L., Nims, C., Theuer, S., Templeton, A.S., Johnson, J.E., 2021. Ferric iron triggers greenalite formation in simulated archean seawater. Geology 49 (8), 905–909.
Isley, A. E., 1995. Hydrothermal Plumes and the Delivery of Iron to Banded Iron Formation.
Isley, A.E., Abbott, D.H., 1999. Plume-related mafic volcanism and the deposition of banded iron formation. J. Geophys. Res. Solid Earth 104 (B7), 15461–15477.
Jamieson, J.W., Wing, B.A., Farquhar, J., Hannington, M.D., 2013. Neoarchaean seawater sulphate concentrations from sulphur isotopes in massive sulphide ore. Nat. Geosci. 6 (1), 61–64.
Jiang, C.Z., Tosca, N.J., 2019. Fe(II)-carbonate precipitation kinetics and the chemistry of anoxic ferruginous seawater. Earth Planet. Sci. Lett. 506, 231–242.
Johnson, C.M., Beard, B.L., Beukes, N.J., Klein, C., O'Leary, J.M., 2003. Ancient geochemical cycling in the Earth as inferred from Fe isotope studies of banded iron formations from the Transvaal Craton. Contrib. Miner. Petrol. 144, 523–547.
Johnson, C.M., Ludois, J.M., Beard, B.L., Beukes, N.J., Heimann, A., 2013. Iron formation carbonates: paleoceanographic proxy or recorder of microbial diagenesis? Geology 41 (11), 1147–1150.
Johnson, C. M., Zheng, X. Y., Djokic, T., Van Kranendonk, M. J., Czaja, A. D., Roden, E. E., and Beard, B. L., 2022a. Early Archean biogeochemical iron cycling and nutrient availability: New insights from a 3.5 Ga land-sea transition. In Earth-Science Reviews (Vol. 228). Elsevier B.V.
Johnson, C. M., Zheng, X. Y., Djokic, T., Van Kranendonk, M. J., Czaja, A. D., Roden, E. E., and Beard, B. L., 2022b. Reply to Comment by Birger Rasmussen and Janet R. Muhling on "Early Archean biogeochemical iron cycling and nutrient availability: New insights from a 3.5 Ga land-sea transition" by Johnson et al. In Earth-Science Reviews (Vol. 231). Elsevier B.V.
Johnson, J.E., Muhling, J.R., Cosmidis, J., Rasmussen, B., Templeton, A.S., 2018. Low-Fe (III) greenalite was a primary mineral from Neoarchean Oceans. Geophys. Res. Lett. 45 (7), 3182–3192.
Klein, C., 2005. Some Precambrian banded iron-formations (BIFs) from around the world: Their age, geologic setting, mineralogy, metamorphism, geochemistry, and origin. In American Mineralogist (Vol. 90, Issue 10, pp. 1473–1499). Mineralogical Society of America.
Konhauser, K. O., Planavsky, N. J., Hardisty, D. S., Robbins, L. J., Warchola, T. J., Haugaard, R., Lalonde, S. V., Partin, C. A., Oonk, P. B. H., Tsikos, H., Lyons, T. W., Bekker, A., and Johnson, C. M., 2017. Iron formations: A global record of Neoarchaean to Palaeoproterozoic environmental history. In Earth-Science Reviews (Vol. 172, pp. 140–177). Elsevier B.V.
Krapež, B., Barley, M.E., Pickard, A.L., 2003. Hydrothermal and resedimented origins of the precursor sediments to banded iron formation: Sedimentological evidence from the Early Palaeoproterozoic Brockman Supersequence of Western Australia. Sedimentology 50 (5), 979–1011.
Krissansen-Totton, J., Arney, G.N., Catling, D.C., 2018. Constraining the climate and ocean pH of the early Earth with a geological carbon cycle model. PNAS 115 (16), 4105–4110.
Kump, L.R., Seyfried, W.E., 2005. Hydrothermal Fe fluxes during the Precambrian: effect of low oceanic sulfate concentrations and low hydrostatic pressure on the composition of black smokers. Earth Planet. Sci. Lett. 235 (3–4), 654–662.
Liu, Z., Rimstidt, J.D., Zhang, Y., Yuan, H., Zhu, C., 2016. A stable isotope doping method to test the range of applicability of detailed balance. Geochem. Perspect. Lett. 2 (1), 78–86.
Lyons, T.W., Tino, C.J., Fournier, G.P., Anderson, R.E., Leavitt, W.D., Konhauser, K.O., Stüeken, E.E., 2024. Co-evolution of early Earth environments and microbial life. Nat. Rev. Microbiol. 1–15.
Maliva, R.G., Knoll, A.H., Simonson, B.M., 2005. Secular change in the Precambrian silica cycle: Insights from chert petrology. Bull. Geol. Soc. Am. 117 (7–8), 835–845.
Miyano, T., Klein, C., 1983. Phase relations of orthopyroxene, olivine, and grunerite in high-grade metamorphic iron-formation. Am. Mineral. 68, 699–716.
Moffett, J.W., German, C.R., 2018. The US GEOTRACES eastern tropical Pacific transect (GP16). Mar. Chem. 201, 1–5.
Muhling, J.R., Gilbert, S.E., Rasmussen, B., 2023. Rare earth element and yttrium (REY) geochemistry of 3.46–2.45 Ga greenalite-bearing banded iron formations: New insights into iron deposition and ancient ocean chemistry. Chem. Geol. 641.
Muhling, J.R., Rasmussen, B., 2020. Widespread deposition of greenalite to form banded iron formations before the great oxidation event. Precambr. Res. 339.
Nagy, K.L., Blum, A.E., Lasaga, A.C., 1991. Dissolution and precipitation kinetics of kaolinite at 80 deg-C and pH 3: the dependence on solution saturation state. Am. J. Sci. 291, 649–686.
Nagy, K.L., Lasaga, A.C., 1992. Dissolution and precipitation kinetics of gibbsite at 80 deg-C and pH 3: the dependence on solution saturation state. Geochim. Cosmochim. Acta 56, 3093–3111.
Nayar, K.G., Sharqawy, M.H., Banchik, L.D., 2016. Thermophysical properties of seawater: a review and new correlations that include pressure dependence. Desalination 390, 1–24.
Nke, A.Y., Tsikos, H., Mason, P.R.D., Mhlanga, X., Tostevin, R., 2024. A seawater origin for greenalite in iron formation. Earth Planet. Sci. Lett. 643.
Posth, N.R., Köhler, I., Swanner, E.D., Schröder, C., Wellmann, E., Binder, B., Konhauser, K.O., Neumann, U., Berthold, C., Nowak, M., Kappler, A., 2013. Simulating Precambrian banded iron formation diagenesis. Chem. Geol. 362, 66–73.
Poulton, S.W., Canfield, D.E., 2011. Ferruginous conditions: a dominant feature of the ocean through Earth's history. Elements 7 (2), 107–112.
Pufahl, P.K., Anderson, S.L., Hiatt, E.E., 2014. Dynamic sedimentation of Paleoproterozoic continental margin iron formation, Labrador Trough, Canada: paleoenvironments and sequence stratigraphy. Sed. Geol. 309, 48–65.
Rasmussen, B., Krapež, B., Muhling, J.R., 2014. Hematite replacement of iron-bearing precursor sediments in the 3.46-b.y.-old Marble Bar Chert, Pilbara craton. Australia. Bulletin of the Geological Society of America 126 (9–10), 1245–1258.
Rasmussen, B., Krapež, B., Muhling, J.R., Suvorova, A., 2015. Precipitation of iron silicate nanoparticles in early Precambrian oceans marks Earth's first iron age. Geology 43 (4), 303–306.
Rasmussen, B., Muhling, J.R., Suvorova, A., Krapež, B., 2016. Dust to dust: evidence for the formation of "primary" hematite dust in banded iron formations via oxidation of iron silicate nanoparticles. Precambr. Res. 284, 49–63.
Rasmussen, B., Muhling, J.R., Suvorova, A., Krapež, B., 2017. Greenalite precipitation linked to the deposition of banded iron formations downslope from a late Archean carbonate platform. Precambr. Res. 290, 49–62.
Rasmussen, B., Muhling, J.R., Tosca, N.J., Tsikos, H., 2019a. Evidence for anoxic shallow oceans at 2.45 Ga: implications for the rise of oxygenic photosynthesis. Geology 47 (7), 622–626.
Rasmussen, B., Muhling, J.R., Fischer, W.W., 2019b. Evidence from laminated chert in banded iron formations for deposition by gravitational settling of iron-silicate muds. Geology 47 (2), 167–170.
Rasmussen, B., Muhling, J.R., 2021. Development of a greenalite-silica shuttle during incursions of hydrothermal vent plumes onto Neoarchean shelf, Hamersley region, Australia. Precambr. Res. 353.
Rasmussen, B., Muhling, J. R., and Krapež, B., 2021. Greenalite and its role in the genesis of early Precambrian iron formations – A review. In Earth-Science Reviews (Vol. 217). Elsevier B.V.
Rasmussen, B., and Muhling, J. R., 2022. Comment on "Early Archean biogeochemical iron cycling and nutrient availability: New insights from a 3.5 Ga land-sea transition" by Clark M. Johnson, Xin-Yuan Zheng, Tara Djokic, Martin J. Van Kranendonk, Andrew D. Czaja, Eric E. Roden, Brian L. Beard, 2022, Earth-Science Reviews., In Earth-Science Reviews (Vol. 231). Elsevier B.V.
Rasmussen, B., Muhling, J.R., Tosca, N.J., Fischer, W.W., 2023. Did nutrient-rich oceans fuel Earth's oxygenation? Geology 51 (5), 444–448.
Rasmussen, B., Muhling, J. R., and Tosca, N. J., 2024a. Nanoparticulate apatite and greenalite in oldest, well-preserved hydrothermal vent precipitates.
Rasmussen, B., Muhling, J.R., Sadekov, A., 2024b. Snapshot of a Paleoarchean seafloor: evidence from 3.43-3.35 Ga Strelley Pool chert-pebble conglomerate for deposition, silicification, and erosion of hydrothermal greenalite-apatite precipitates. Precambr. Res. 412.
Resing, J.A., Sedwick, P.N., German, C.R., Jenkins, W.J., Moffett, J.W., Sohst, B.M., Tagliabue, A., 2015. Basin-scale transport of hydrothermal dissolved metals across the South Pacific Ocean. Nature 523 (7559), 200–203.
Rimstidt, J.D., 1997. Quartz solubility at low temperatures. Geochim. Cosmochim. Acta 61 (13), 2553–2558.
Rimstidt, J.D., 2014. Geochemical rate models: an introduction to geochemical kinetics. Cambridge University Press, Cambridge, UK.
Robbins, L.J., Swanner, E.D., Lalonde, S.V., Eickhoff, M., Paranich, M.L., Reinhard, C.T., Peacock, C.L., Kappler, A., Konhauser, K.O., 2015. Limited Zn and Ni mobility during simulated iron formation diagenesis. Chem. Geol. 402, 30–39.
Robbins, L.J., Lalonde, S.V., Planavsky, N.J., Partin, C.A., Reinhard, C.T., Kendall, B., Scott, C., Hardisty, D.S., Gill, B.C., Alessi, D.S., Dupont, C.L., Saito, M.A., Crowe, S. A., Poulton, S.W., Bekker, A., Lyons, T.W., Konhauser, K.O., 2016. Trace elements at the intersection of marine biological and geochemical evolution. Earth Sci. Rev. 163, 323–348.
Schott, J., Saldi, G.D., Zhu, C., Gong, L., Chen, K., 2024. Mechanisms controlling albite dissolution/precipitation kinetics as a function of chemical affinity: New insights from experiments in 29Si spiked solutions at 150 and 180 °C. Geochim. Cosmochim. Acta.
Sharqawy, M.H., Lienhard, J.H., Zubair, S.M., 2010. Thermophysical properties of seawater: a review of existing correlations and data. Desalin. Water Treat. 16 (1–3), 354–380.
Siever, R., 1992. The silica cycle in the Precambrian. Geochim. Cosmochim. Acta 56 (8), 3265–3272.
Sun, S., Konhauser, K.O., Kappler, A., Li, Y.L., 2015. Primary hematite in Neoarchean to Paleoproterozoic oceans. Bull. Geol. Soc. Am. 127 (5–6), 850–861.
Sylvestre, G., Evine Laure, N.T., Gus Djibril, K.N., Arlette, D.S., Cyriel, M., Timoléon, N., Jean Paul, N., 2017. A mixed seawater and hydrothermal origin of superior-type banded iron formation (BIF)-hosted Kouambo iron deposit, Palaeoproterozoic Nyong series, Southwestern Cameroon: constraints from petrography and geochemistry. Ore Geol. Rev. 80, 860–875.
Tosca, N.J., Guggenheim, S., Pufahl, P.K., 2016. An authigenic origin for Precambrian greenalite: Implications for iron formation and the chemistry of ancient seawater. Bull. Geol. Soc. Am. 128 (3–4), 511–530.
Tosca, N.J., Jiang, C.Z., Rasmussen, B., Muhling, J., 2019. Products of the iron cycle on the early Earth. In: Free Radical Biology and Medicine, Vol. 140. Elsevier Inc., pp. 138–153
Tosca, N.J., Macdonald, F.A., Strauss, J.V., Johnston, D.T., Knoll, A.H., 2011. Sedimentary talc in Neoproterozoic carbonate successions. Earth Planet. Sci. Lett. 306 (1–2), 11–22.

Tosca, N.J., Tutolo, B.M., 2023. Hydrothermal vent fluid-seawater mixing and the origins of Archean iron formation. Geochim. Cosmochim. Acta 352, 51–68.
Tostevin, R., Ahmed, I.A.M., 2023. Micronutrient availability in Precambrian oceans controlled by greenalite formation. Nat. Geosci. 16, 1188–1193.
Tostevin, R., Sevgen, S., 2024. The role of Fe(II)-silicate gel in the generation of Archean and Paleoproterozoic chert. Geology.
Trendall, A. F., 2002. The Significance of Iron-Formation in the Precambrian Stratigraphic Record. In Precambrian Sedimentary Environments (pp. 33–66). Wiley.
Tutolo, B.M., Tosca, N.J., 2018. Experimental examination of the Mg-silicate-carbonate system at ambient temperature: Implications for alkaline chemical sedimentation and lacustrine carbonate formation. Geochim. Cosmochim. Acta 225, 80–101.
Viehmann, S., Bau, M., Hoffmann, J.E., Münker, C., 2015. Geochemistry of the Krivoy Rog Banded Iron Formation, Ukraine, and the impact of peak episodes of increased global magmatic activity on the trace element composition of Precambrian seawater. Precambr. Res. 270, 165–180.
Yücel, M., Gartman, A., Chan, C.S., Luther, G.W., 2011. Hydrothermal vents as a kinetically stable source of iron-sulphide-bearing nanoparticles to the ocean. Nat. Geosci. 4 (6), 367–371.
Yücel, M., Sevgen, S., Le Bris, N., 2021. Soluble, colloidal, and particulate iron across the hydrothermal vent mixing zones in broken spur and rainbow, mid-atlantic ridge. Front. Microbiol. 12.
Zhang, Y., Gong, L., Chen, K., Burkhart, J., Yuan, H., Zhu, C., 2020. A method for Si isotope tracer kinetics experiments: Using Q-ICP-MS to obtain 29Si/28Si ratios in aqueous solutions. Chem. Geol. 531.
Zhu, C., Liu, Z., Zhang, Y., Wang, C., Scheafer, A., Lu, P., Zhang, G., Georg, R.B., lin Yuan, H., Rimstidt, J.D., 2016. Measuring silicate mineral dissolution rates using Si isotope doping. Chem. Geol. 445, 146–163.
Zhu, C., Zhang, Y., Rimstidt, J.D., Gong, L., Burkhart, J.A.C., Chen, K., Yuan, H., 2021. Testing hypotheses of albite dissolution mechanisms at near-equilibrium using Si isotope tracers. Geochim. Cosmochim. Acta 303, 15–37.